# Study of the Effect of Low-Energy Irradiation with $O^{2+}$ Ions on Radiation Hardening and Modification of the Properties of Thin $TiO_2$ Films

A. Kozlovskiy[1,2] · D. Shlimas[1,2] · I. Kenzhina[1,2] · O. Boretskiy[3] · M. Zdorovets[1,2,4]

## Abstract

The paper presents the results of a systematic study of the effect of exposure to low-energy $O^{2+}$ ions on the structural, optical, mechanical properties, as well as resistance to degradation and aging of thin $TiO_2$ films. The studied samples were obtained using the magnetron sputtering method; the film thickness was 600 nm. Atomic force and scanning electron microscopy, energy dispersive analysis, X-ray diffraction, and UV–Vis spectroscopy were used as the main research methods. In the course of the results, dose dependences of changes in the properties of thin films were established, and it was also shown that irradiation leads to an increase in hardness and resistance to cracking due to radiation hardening. A decrease in the band gap from 3.61 to 3.43 eV not only changes the optical properties, but also has a significant effect on the change in the conductivity. The novelty and relevance of this study lies not only in obtaining new data on the effect of ionizing radiation on the properties of thin films, but also in expanding the prospects for the use of ion irradiation for the purpose of radiation hardening and modification of new materials.

**Keywords** Thin films · Radiation modification · Hardness · Band gap · $TiO_2$

## 1 Introduction

To date, interest in group IV-VI semiconductor thin films (ZnO, CdSe, $TiO_2$, CdTe, $SnO_2$) [1–4] is due to their structural properties, as well as a sufficiently small band gap of 2.5–4.0 eV, which makes them one of the most promising materials as photocatalysts [5, 6], alternative power supplies and batteries [7–9], biomedicine and pharmaceuticals [10, 11]. At the same time, a huge amount of scientific research is aimed at studying the possibility of changing the properties of thin films in order to increase the efficiency of their use. The greatest progress in this direction is associated with the effects of doping thin films with various elements including rare earths [12–16]. The basis

of this method is the use of various precursors, which are dopants, and their addition either in the initial solutions or in the process of spraying. In most cases, this technique leads to unique results in increasing the efficiency of using semiconductor films in photocatalysis by increasing not only photocatalytic activity, but also recycling [17, 18], in biomedicine by increasing antibacterial properties [19], increasing anticorrosion properties and strength characteristics [20]. However, despite all the advantages of this doping method, great difficulties arise with its implementation and scalability on an industrial scale. One of the competing methods for increasing the efficiency of the properties of semiconductor structures is exposure to low-energy beams of either high power [21–23] or large doses of radiation [22, 24, 25]. In turn, the application of these irradiation methods has established itself as one of the most promising methods for changing the properties of materials to a given depth and in a wide range of structural and mechanical parameters by varying both the ion beam energy and the dose dependence. Moreover, in contrast to standard doping methods, in which the effective distribution of the dopant in the structure can be both isotropic and anisotropic, in the case of ion beams, the effective depth of

✉ A. Kozlovskiy
kozlovskiy.a@inp.kz

1 The Institute of Nuclear Physics, Almaty, Kazakhstan

2 L.N. Gumilyov, Eurasian National University, Nur-Sultan, Kazakhstan

3 Al-Farabi Kazakh National University, Almaty, Kazakhstan

4 Ural Federal University, Yekaterinburg, Russia

the dopant and its concentration can be varied with high accuracy. In this regard, in recent years, more and more attention has been paid to studies aimed at assessing the efficiency of using low-energy beams for ionic modification of various structures, including semiconductor thin films [26–35].

The purpose of this scientific work is to study the effect of doping with low-energy $O^{2+}$ ions on structural, optical, mechanical properties, as well as resistance to degradation and aging. The novelty and relevance of this study lies not only in obtaining new data on the effect of ionizing radiation on the properties of thin films, but also in expanding the prospects for the use of ion irradiation for the purpose of radiation hardening and modification of new materials.

The choice of thin films based on titanium dioxide (TiO$_2$) as the object of study and further modification of its properties is due to its wide application not only as industrial protective coatings, microelectronic and optical devices, but also to its great interest in the field of photocatalysis, solar cells, pharmaceuticals, etc., for which one of the important properties is the effective specific surface area, as well as the band gap.

## 2 Experimental Part

### 2.1 Initial Samples

TiO$_2$ thin films were selected as the test samples. To obtain thin films, the magnetron sputtering method was applied using the Edwards Auto 500 (BOC Edwards, Burgess Hill, England) setup [36]. The thickness of the obtained films was monitored by raster electron microscopy and ellipsometry. The obtained value was $600 \pm 5$ nm. A detailed description of the technique for producing thin films is presented in [36].

### 2.2 Modification of the Properties of Thin TiO$_2$ Films

Modification of the initial films in order to determine the possibility of using ionizing radiation to change the physicochemical properties of thin films was carried out by irradiation with low-energy $O^{2+}$ ions with an energy of 20 keV/charge. Irradiation was carried out on a DC-60 heavy ion accelerator (Nur-Sultan, Kazakhstan). The radiation doses were $10^{13}$–$10^{16}$ ion/cm$^2$ [37]. In order to avoid the effect of local heating during irradiation, the targets were placed on a cooling substrate, which maintained the temperature of the target in the range of 23–25 °C. According to the calculated data, the energy loss is $dE/dx_{Elec.} = 240 \pm 10$ eV/nm, a $dE/dx_{nuclear} = 170 \pm 10$ eV/nm, the maximum ion mean free path does not exceed 350 nm.

## 2.3 Investigation of the Physicochemical Properties of Thin TiO$_2$ Films

The influence of the dose load on the change in the topology of the surface of thin films, as well as the degree of roughness and waviness, was determined by analyzing 3D images obtained using the atomic force microscopy method. The studies were performed on an STM SmartSPM atomic force microscope (AIST-NTLtd, Novato, CA, USA). Scan mode: AC-Mode (Non-Contact Mode); Scan rate/scan frequency 0.4 Hz, Resolution XY 700×700, Scan size XY 5×5 um, Z is automatic; Cantiliver tip: The radius curvature of the sharp cantiliver is less than 10 nm.

The study of the effect of irradiation on the change in structural properties was carried out using the method of x-ray diffraction, by constructing diffraction patterns of the samples before and after irradiation, as well as an analytical comparison of the observed changes. The instrument base is D8 ADVANCE ECO (Bruker, Karlsruhe, Germany), shooting mode: Bragg–Brentano geometry, CuKα = 1.5406 Å, measurement range—2θ = 40°–80°, step 0.02°, shooting time 3 s at a point. The choice of the angular measurement range 2θ = 40°–80° is due to the absence of diffraction reflections related to the TiO$_2$ phase in the region below 2θ = 40°. The assessment of the structural parameters, including the parameters of the crystal lattice, distortions, and dislocation density were calculated using the DiffracEVA and TOPAS v.4 software codes, which are used to interpret X-ray diffraction patterns. The analysis of the influence of the size factor and the distorting factor on the change in the shape and intensity of diffraction lines was carried out by means of a full-profile analysis of diffraction patterns by the Rietveld method.

The elemental composition in thin films was determined before and after irradiation using the energy dispersive analysis method performed on a «Hitachi TM3030» scanning electron microscope (Hitachi Ltd, Chiyoda, Tokyo, Japan) with a «Bruker XFlash MIN SVE» microanalysis system (Bruker, Karlsruhe, Germany).

The optical properties as well as the band gap were obtained by measuring the UV–Vis spectra with a Jena Specord-250 BU analytical spectrophotometer (Analytik Jena, Jena, Germany). Diffuse reflectance UV–Vis spectra were recorded using equipped with integrating sphere. The resolution was chosen to be 0.5 nm and the scan speed was 1 nm/s. The spectral range was from 300 to 800 nm. The measurement was carried out in the transmission mode.

### 2.4 Mechanical Tests and Determination of Crack Resistance

The study of microhardness was carried out using the nanoindenter method. The Vickers diamond pyramid was

used as an indenter. To determine changes in hardness with depth, we used the method of variable loading on the indenter in the range from 10 to 1000 N. The value of microhardness for $TiO_2$ films, according to the literature, varies from 300 to 650–700 HV and strongly depends on the method of obtaining thin films [38–40].

The kinetics of artificial accelerated aging in order to determine the dynamics of changes in the properties of thin films and crack resistance was carried out using the methodology of modeling the external effects of water vapor at a temperature of 150 °C and a pressure of 2.2–2.3 atm. These conditions of modeling the aging effect allow for 1 h of exposure to age the sample in time comparable to the aging effect for 1.5–2.0 years under natural exposure [41–43].

The determination of the dry friction coefficient was carried out using the method of translational sliding (10%) of a ceramic ball with a diameter of 3 mm at a load of 100 N. The number of test cycles was 20,000. At various stages, the values of the dry friction coefficient were determined, as well as the volume loss of coatings.

## 3 Results and Discussion

### 3.1 Analysis of Structural Characteristics and Degree of Texturing

Figure 1 shows the results of x-ray diffraction of the studied thin $TiO_2$ films before and after ion modification. According to the full-profile analysis of X-ray diffraction patterns, it was found that the obtained samples are polycrystalline structures with reflections and crystal lattice parameters characteristic of the orthorhombic phase of brookite. An analysis of the intensities and shapes of diffraction reflections indicates the presence of a small content of distortions in the lattice structure, as well as the identified orientation directions of the texture planes along the axes (420) and (104). The presence of two selected textures indicates the distortion of grains in the structure and different orientations. An analysis of the FWHM values using the Williamson-Hall method [44] showed that, in the case of the initial films, the dimensional factor has a distortion in the shape of the lines. To determine the phase composition of the



**Fig. 1** **a** Dynamics of X-ray diffraction patterns of the studied samples of thin films; **b** Graph of the angular dependence of the change in FWHM for the samples under study
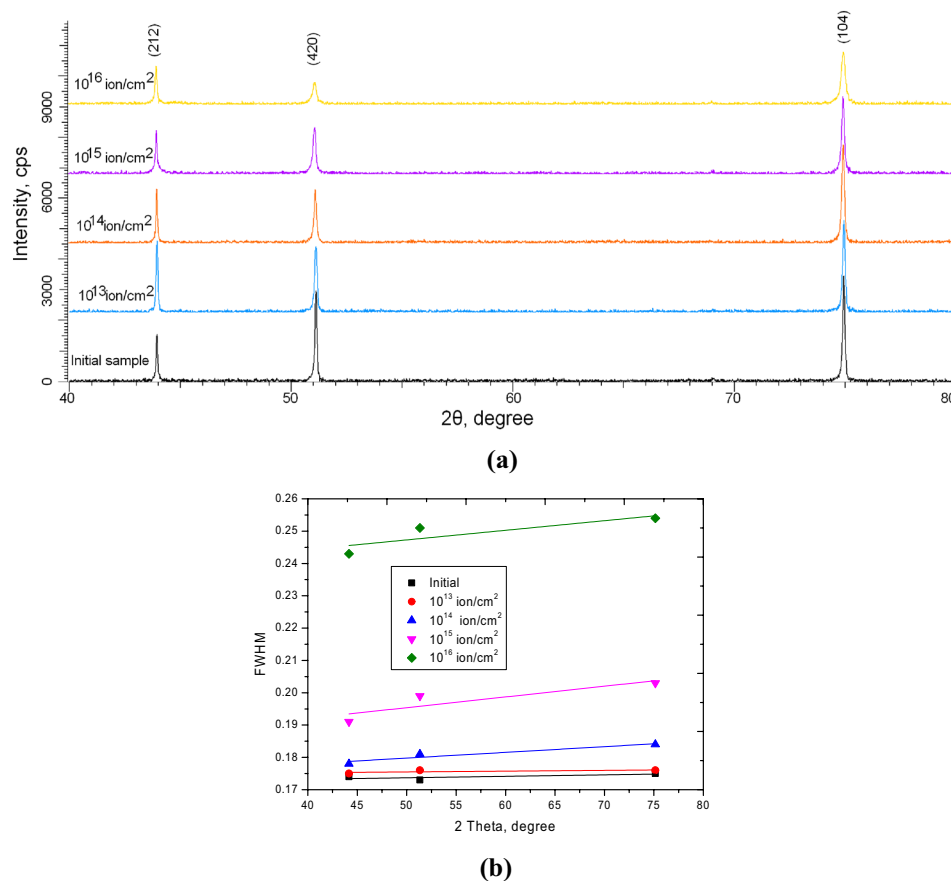
samples under study, the PDF-2 database was used; PDF-01-076-1934 was used as a card for clarifying the structural parameters.

The dislocation density ($\delta$) was calculated using the formula (1) [45]:

$$\delta = \frac{1}{L^2}, \tag{1}$$

where L = crystallite size, nm.

For irradiated samples at irradiation doses of $10^{13}$–$10^{14}$ ion/cm$^2$, structural changes associated with changes in crystallite sizes, as well as distortion and macrostresses (changes in interplanar spacings and their deformations) are within the error. However, for these samples, a change in the intensity of diffraction reflections is observed, which indicates a reorientation of the textures in the films and the formation of an equally probable orientation of the grains in the structure. An increase in the radiation dose to $10^{15}$–$10^{16}$ ion/cm$^2$ leads to a sharp decrease in grain sizes, which indicates the processes of recrystallization and partial fragmentation of grains, as well as an increase in deformations and dislocation density (see Table 1). A similar character of the change in structural quantities at high radiation doses, as well as the reorientation of texture planes, can be caused by radiation damage processes and the formation of a large number of overlapping regions of ion paths in the film structure at high fluences [46]. In the case where the probability of overlapping trajectories of radiation damage during the passage of ions in the material is 100–1000 times, regions with strong disordering or altered electron density can arise in the structure due to cascade effects of knocked out secondary electrons or primary knocked out atoms. In this case, irradiation with large fluences can lead to partial doping of $O^{2+}$ ions into the sites and vacancy voids of the crystal lattice, thereby changing it. According to the calculated data, the percentage of doped $O^{2+}$ ions depending on the fluence is from 0.000033 to 0.04%, which is a fairly significant value at high fluences. It is also worth noting that, due to the low energy of incident ions, the energy losses

due to elastic collisions (interactions with electron shells) and inelastic collisions (interactions with target nuclei) are comparable in magnitude, and, therefore, the probabilities of the formation of electronic cascades as a result of interactions and the formations of initially knocked out atoms are also comparable in magnitude. However, due to the different masses and atomic radii of titanium (47.8 amu and 147 pm) and oxygen (15.99 amu and 60 pm), as well as binding energies, knocking out of oxygen atoms from equilibrium positions is greater, than titanium atoms, and because of this, a change in the stoichiometric ratio of oxygen and titanium in the structure of the surface layer can be observed in the structure (see Table 1). At the same time, a detailed analysis of the distribution of elements showed that with an increase in the radiation dose, the formation of regions containing a greater amount of oxygen becomes larger, and these regions themselves form near the largest accumulation of defective regions on the surface. The density of structural disorder was calculated using formula (2):

$$f_d(\varphi t) = \frac{M(\varphi t) - M_0}{M_s - M_0}, \tag{2}$$

where $M(\varphi t)$ = defect concentration, measured quantity as a function of ion fluence, $M_0$ = defect concentration before irradiation, $M_s$ = maximum concentration of defects in irradiated samples, $\varphi$ = fluence, ion/m$^2$, $t$ = exposure time.

## 3.2 The Study of the Surface Topography of Thin Films

Figure 2 presents the results of changes in the surface morphology of thin films as a result of irradiation with $O^{2+}$ ions with different doses, as well as data on the degree of roughness and waviness depending on the radiation dose.

As can be seen from the data presented, in the case of the initial samples, the surface topography of the thin films has a relatively smooth structure, without any inclusions or formations. The degree of roughness and waviness (see Fig. 2f) for

**Table 1** Data of structural parameters

| Parameter | Fluence, ion/cm$^2$ | | | | |
| --- | --- | --- | --- | --- | --- |
| | Initial | $10^{13}$ | $10^{14}$ | $10^{15}$ | $10^{16}$ |
| Density of structural disorder, % | 0.31 | 0.37 | 1.31 | 1.93 | 2.54 |
| Crystalline size, nm | 54±3 | 53±2 | 51±3 | 46±2 | 32±5 |
| Dislocation density, $10^{11}$ 1/cm$^2$ | 0.35 | 0.36 | 0.39 | 0.46 | 0.93 |
| Macrostrain | 0.032 | 0.036 | 0.041 | 0.056 | 0.081 |
| Lattice parameter, Å | a=9.2025, b=5.6307, c=5.1019 | a=9.2031, b=5.6356, c=5.1114 | a=9.2038, b=5.6386, c=5.1252 | a=9.2154, b=5.6425, c=5.1653 | a=9.2241, b=5.6842, c=5.1943 |
| The ratio of the Ti/O elements | 33.5/66.5 | 33.2/66.8 | 31.3/68.7 | 29.1/70.9 | 28.3/71.7 |
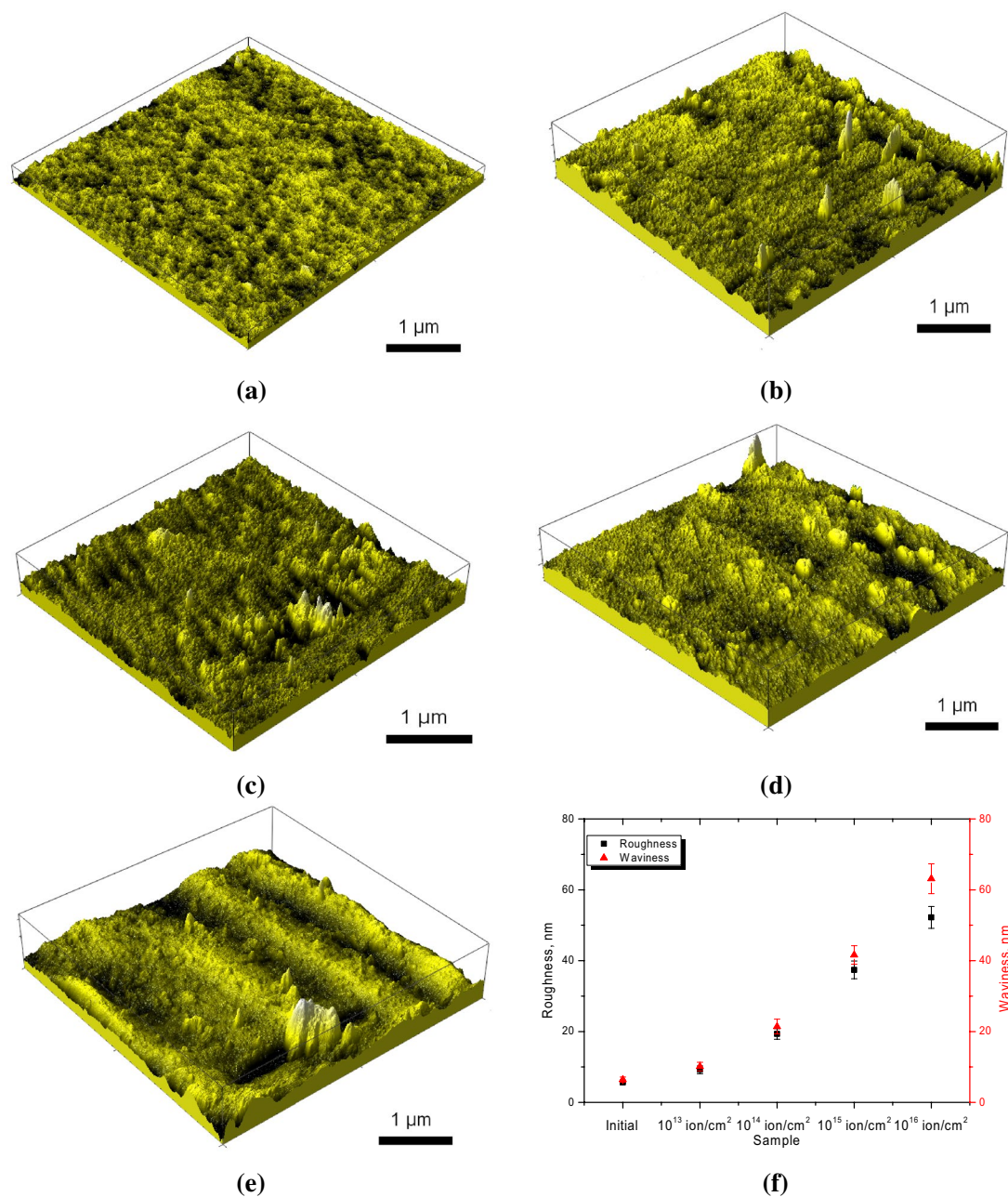
**Fig. 2** Images of the surface topography of thin films before and after irradiation: **a** initial; **b** $10^{13}$ ion/cm$^2$; **c** $10^{14}$ ion/cm$^2$; **d** $10^{15}$ ion/cm$^2$; **e** $10^{16}$ ion/cm$^2$; **f** Dynamics of changes in the waviness and roughness of thin films before and after irradiation

the initial samples are quite small and do not exceed 5–7 nm. The obtained data on the surface topography of the initial films indicate the isotropy of the deposition and formation of films under the selected synthesis conditions.

For irradiated samples, the formation of horse-shaped hillocks is observed on the surface of the films, the density and dimensions of which increase with the radiation dose. The formation of hillocks as a result of the accumulation of radiation defects in the structure during irradiation was first explained by Evans during the accumulation of helium in the

metal structure as a result of irradiation [47]. According to this mechanism, a certain number of defects accumulate in the structure of the surface layer, which, as a result of accumulation, creates excessive pressure and stress on the crystal lattice. With an increase in the irradiation dose, the number of defective areas increases and, consequently, the degree of distortion and stress near the grain boundaries also grows, a further increase in which leads to swelling and extrusion of the defective volume to the surface.

Also, at high radiation doses, partial spraying of the surface layer can be observed, which leads to the formation of wave-like inclusions on the surface of the films (see Fig. 2d, e).

Thus, the main topographic changes during irradiation with low-energy $O^{2+}$ ions are the formation of hillocks (doses of $10^{13}$–$10^{14}$ ion/cm$^2$) and wave-like inclusions (doses of $10^{15}$–$10^{16}$ ion/cm$^2$), which leads to an increase in surface roughness and waviness. Also, as mentioned earlier, in the vicinity of these inclusions, an increased content of oxygen atoms is observed.

## 3.3 Optical and Conductive Properties

Figure 3 presents UV–Vis spectroscopy data, in particular, the transmission spectra of TiO$_2$ and Tauc's plot thin films, on the basis of which the dependences of the variation in the band gap were obtained.

According to the data of transmission spectra, it was found that the transparency of the initial films is 89–91% in the visible region, which indicates good optical properties of the films. Irradiation with doses of $10^{13}$–$10^{14}$ ion/cm$^2$ leads to a slight decrease in transparency to 78–85%, which is due to a change in the topography of the surface of thin films as a result of irradiation and deformation of the crystal structure. Moreover, the vibrational nature of the spectrum indicates the uniformity and isotropy of the thickness of the films in the initial state and irradiated with doses of $10^{13}$–$10^{14}$ ion/cm$^2$. The formation of wavy inclusions, an increase in the degree of roughness and waviness leads to a decrease in the transparency of thin films from 89% for initial samples to 57–64% for samples irradiated with doses of $10^{15}$–$10^{16}$ ion/cm$^2$. In this case, a change in the vibrational nature of the transmission spectra indicates a change in the isotropy of the film thickness as a result of a strong change in the surface topography.

Analyzing the obtained spectra, we can distinguish three characteristic regions. The region of 300–400 nm, which corresponds to strong absorption and, as a rule, is used to construct the Tauc's plot and determine the magnitude of the band gap. The region of 400–550 nm, corresponding to the absorption of the medium, and describing the degree of ordering and disordering of the films. The region of 550–800 nm is the region of weak absorption, which arises as a result of the formation of point defects and impurity inclusions during irradiation. Moreover, for samples irradiated with doses of $10^{15}$–$10^{16}$ ion/cm$^2$ leads to a strong predominance of the region of weak absorption and a significant expansion of its boundaries. Based on the obtained transmission spectra, the band gap and their dynamics as a result of irradiation were determined. The optical band gap Eg was calculated using formula (3) [48]:

$$\alpha = A(h\nu - E_g)^{1/2} \tag{3}$$

where $\alpha$ – the absorption coefficient defined by the Beer-Lambert law, $A$ is a energy-independent constant and $h\nu$ is the photon energy, $E_g$ is band gap. The absorption coefficient is determined by analyzing the obtained UV–Vis spectra.

The oscillator energy ($E_0$) is determined using the formula (4) [48]:

$$E_0 = 1.5 * E_g^{W-D} \tag{4}$$

The refractive index (n) dispersion of TiO$_2$ thin films can be analyzed by the Wemple–DiDomenico (W–D) single effective-oscillator model (5) [48]:

$$n^2(h\nu) = 1 + \frac{E_d * E_0}{E_0^2 - (h\nu)^2} \tag{5}$$

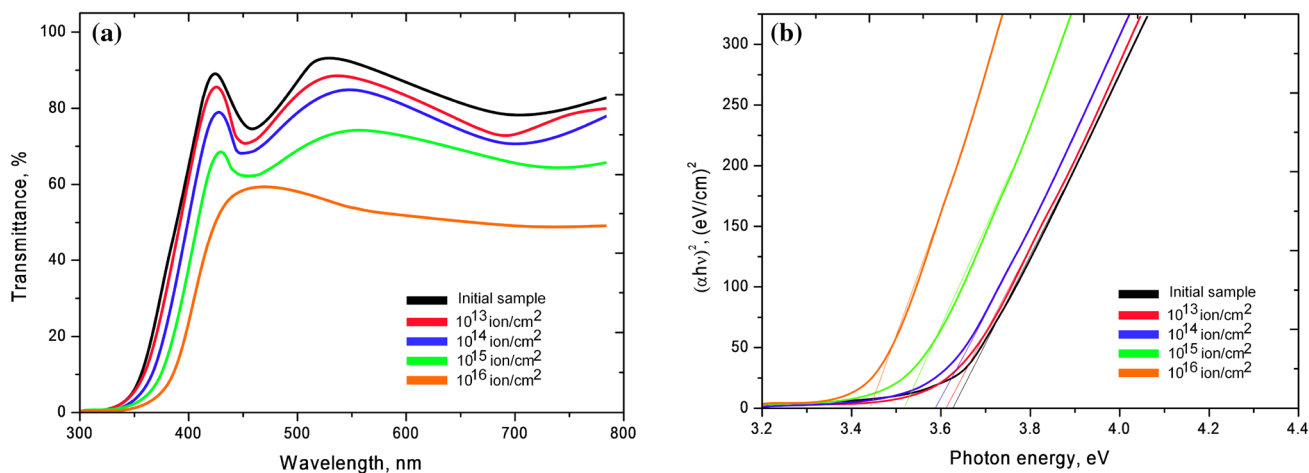where $E_d$ is the dispersion parameter, $E_0$ is oscillator energy.



**Fig. 3** **a** Transmittance spectra of samples TiO$_2$ thin films; **b** Tauc's plot

The results of the obtained optical data, such as high frequency dielectric constant ($\varepsilon_\infty$), band gap ($E_g$), the dispersion parameter ($E_d$), oscillator energy ($E_0$), are presented in Table 2.
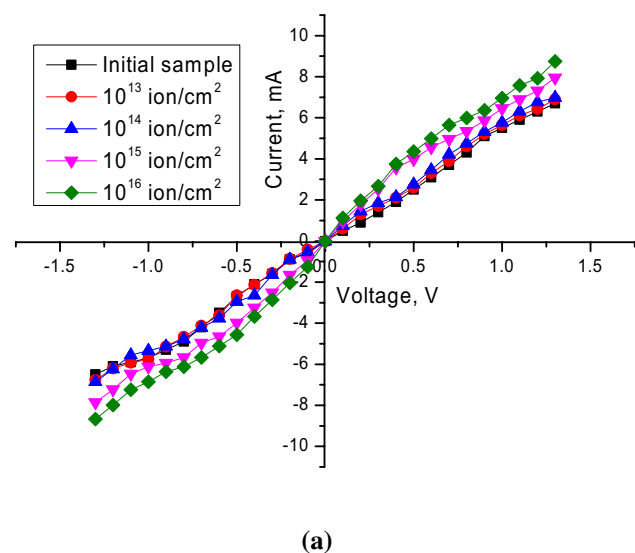
The change in the band gap depending on the radiation dose is of a two-stage nature. The first stage is typical for doses of $10^{13}$–$10^{14}$ ion/cm$^2$, when the change in the band gap is minimal. The second stage, which is characterized by a strong decrease in the band gap, is characteristic of maximum radiation doses. A decrease in the band gap indicates a change in the Ti–O, O–O bond lengths, as well as a change in the dislocation density of defects and grain sizes. A similar behavior is observed for the value of oscillator energy. While the parameters $\varepsilon_\infty$ and $E_d$ tend to increase depending on the radiation dose.

Figure 4 presents the data on changes in the current—voltage characteristics of thin TiO$_2$ films depending on the radiation dose, as well as a graph of the conductivity obtained as a result of the analysis of the current—voltage characteristics. The general view of the obtained current—voltage characteristics indicates the ohmic nature of the conductivity of thin films. In this case, an increase in the radiation dose leads to an increase in the slope of the I–V characteristic, which indicates an increase in the specific conductivity, the dynamics of which are presented in Fig. 4b.

As is known, TiO$_2$ in general is an indirect semiconductor with n-type conductivity, as well as due to the small size of crystallites and their subsequent reduction as a result of irradiation, a changed band gap. Moreover, in the case of changes in the oxygen concentration and its distribution in the crystal lattice as a result of irradiation, due to the displacement of oxygen atoms from the lattice sites, additional oxygen vacancies can form in the structure. These vacancies are capable of occupying titanium atoms by oxidation from $+4$ to $+3$, which also shift from their positions as a result of irradiation. The resulting Ti$^{3+}$ ions, in this case, in the crystal lattice behave as electron donors, thereby providing a donor type of conductivity and forming local states near the bottom of the conduction band, thereby increasing the conductivity. Also, a change in the Ti–O, O–O bond wavelength, which leads to a decrease in the band gap, has an effect on the conductive properties and bonding forces in electronic orbitals.

### 3.4 Mechanical and Strength Tests

These changes in the dynamics of the hardness of thin films in depth depending on the radiation dose, as well as the degree of hardening of thin films as a result of irradiation are shown in Fig. 5. For the initial sample, the change in hardness depending on the penetration depth of the indenter is almost linear, which indicates the uniformity
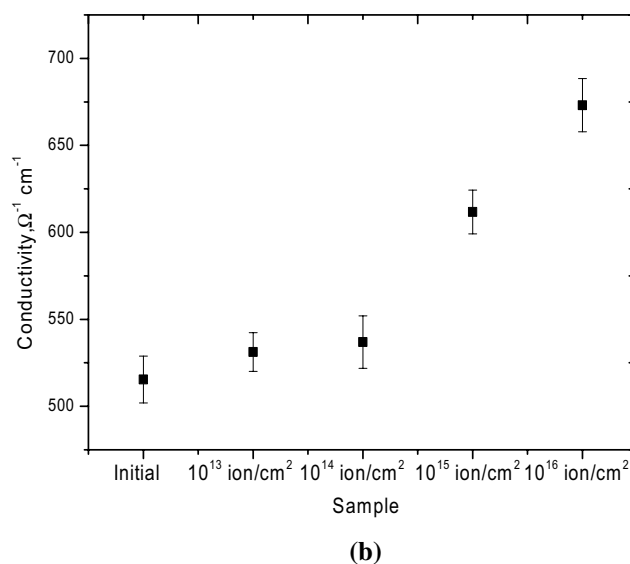
**Table 2** Data on changes in optical characteristics of tested samples depending on radiation dose

| Sample | $\varepsilon_\infty$ | $E_g$ | $E_d$, eV | $E_0$, eV | $E_d/E_0$ |
|---|---|---|---|---|---|
| Initial | 4.76 | 3.61 | 11.33 | 5.42 | 2.09 |
| $10^{13}$ ion/cm$^2$ | 4.84 | 3.60 | 11.52 | 5.40 | 2.13 |
| $10^{14}$ ion/cm$^2$ | 4.99 | 3.58 | 11.91 | 5.37 | 2.22 |
| $10^{15}$ ion/cm$^2$ | 5.54 | 3.51 | 13.27 | 5.27 | 2.52 |
| $10^{16}$ ion/cm$^2$ | 6.19 | 3.43 | 14.85 | 5.15 | 2.89 |

$\varepsilon_\infty$ High frequency dielectric constant, $E_g$ band gap, $E_d$ the dispersion parameter, $E_0$ oscillator energy



**(a)**



**(b)**

**Fig. 4** **a** IVC plots of test samples; **b** Graph of changes in the conductivity of the test samples

of thin films. A slight decrease at a depth of 550–600 nm is due to the fact that this layer is the primary layer during the deposition of films which provides both adhesion on the surface of the substrate and further nucleation of grains on the surface of the substrate. The general view of the depth variation in the hardness of thin films is of two stages for all irradiated samples. For samples irradiated with a dose of $10^{13}$ ions/cm$^2$, the change in the hardness value is practically not observed, which is due to the small contribution of structural changes caused by irradiation. An increase in the radiation dose above $10^{14}$ ion/cm$^2$ leads to an increase in hardness, which indicates hardening of the near-surface layer 350–400 nm thick, which is characteristic of the maximum ion mean free path in thin films. The characteristic decline after 350–400 nm is due to the fact that the main hardening processes are observed near the ion path, and all hardening effects observed at a greater depth can be due to cascading effects of defect migration as a result of the accumulation of large doses of radiation. The presented diagram of the degree of hardening of thin films as a result of irradiation (see Fig. 5b) clearly reflects the change in the value of hardening depending on the dose, according to which the greatest increase in hardening is observed for samples irradiated with a dose of $10^{15}$ ion/cm$^2$, and a further increase in the radiation dose, although this leads to an increase strength, but is associated with large changes in surface topography, which can have both a positive and negative effect during operation. The change in hardness depending on the radiation dose is directly related to the change in the density of dislocations and defects in the structure. At low irradiation fluences ($10^{13}$–$10^{14}$ ion/cm$^2$), when the effect of overlapping the

trajectories of ions in the films is small, not exceeding 10–100 times, the dislocation concentration remains practically unchanged (see Data in Table 1). An increase in the irradiation dose to $10^{15}$–$10^{16}$ ion/cm$^2$ leads to a sharp increase in the overlap effect, which can lead not only to an increase in defects in the structure, but also to recrystallization processes associated with the fragmentation of grains or their reorientation, as well as the implantation of ions into films. As a result, an increase in the dislocation density is observed by a factor of 1.5–3, depending on the irradiation fluence. An increase in dislocation density in some cases leads to hardening of the near-surface layer, which is observed in the data shown in Fig. 5.

The results of wear resistance obtained by determining the coefficient of dry friction depending on the number of test cycles are presented in Fig. 6.

As can be seen from the data presented, a change in surface topography as a result of the accumulation of the radiation dose leads to an increase in the dry friction coefficient. However, the dynamics of cyclic tests shows that in the case of irradiated samples, a change in the dry friction coefficient is practically not observed, while for the initial sample and irradiated with doses of $10^{13}$–$10^{14}$ ion/cm$^2$, this value has a tendency to increase after 7000–10,000 test cycles, which indicates surface deterioration due to friction. In the case of samples irradiated with doses of $10^{15}$–$10^{16}$ ions/cm$^2$, which are characterized by an increase in hardness due to a change in the density of dislocations, a change in the value of the dry friction coefficient is practically not observed, which indicates an increased resistance of the irradiated films to cracking.
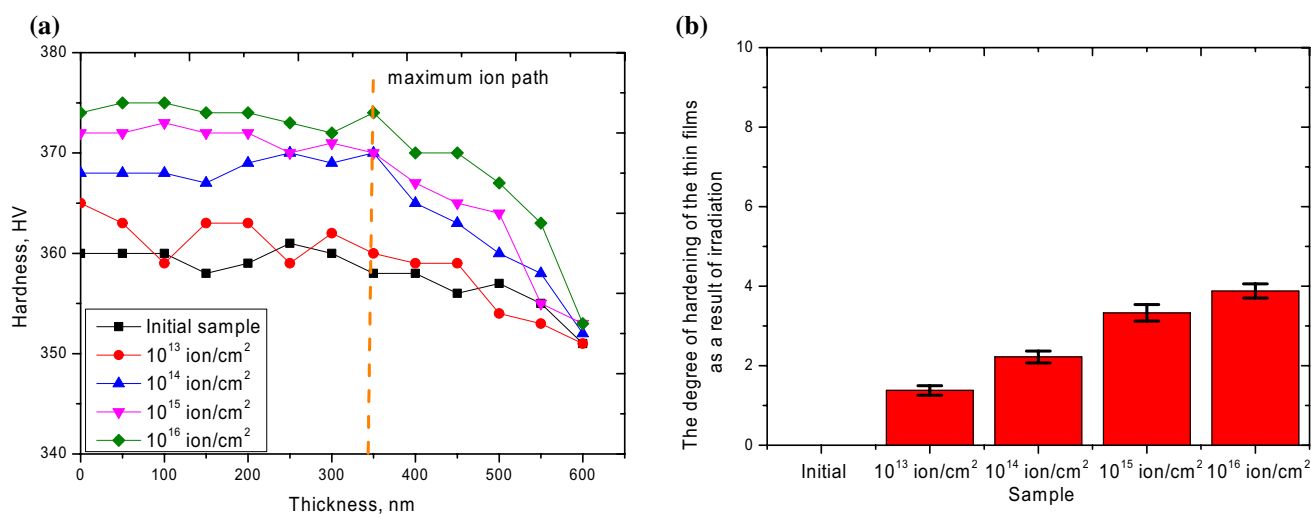


Fig. 5 a Graph of variation of microhardness of tested samples depending on radiation dose; b Diagram of the degree of hardening of thin films as a result of irradiation
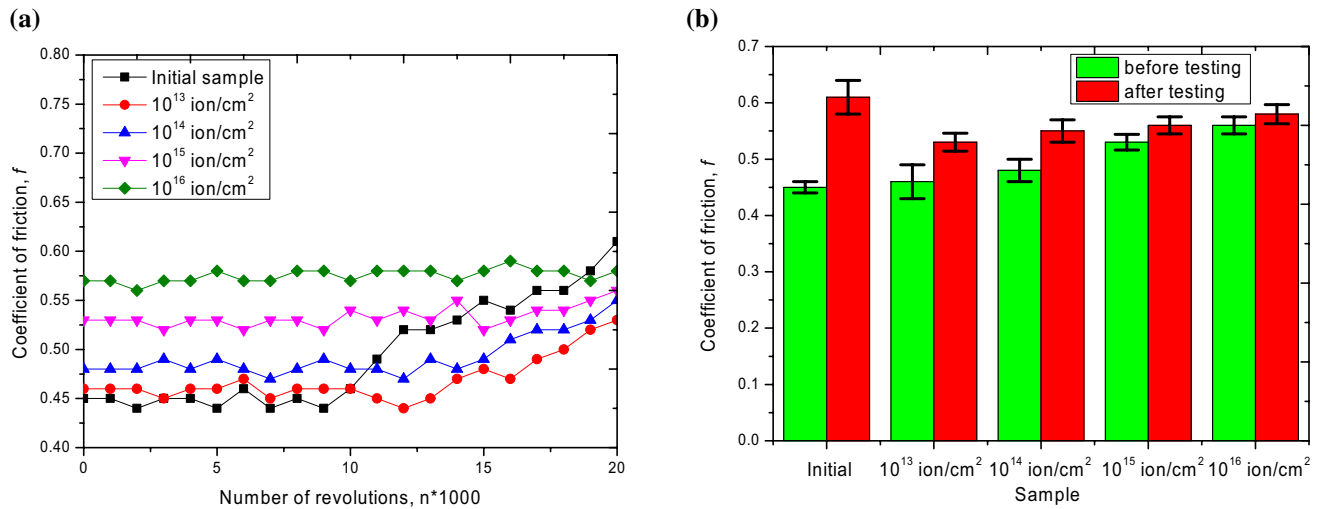
**(a)**



**(b)**



**Fig. 6** **a** The dependence of the change in the coefficient of dry friction on the number of test cycles; **b** comparative diagram of changes in the coefficient of dry friction before and after tests

### 3.5 Modeling of the Aging Effect and Change in the Crack Resistance of Thin TiO$_2$ Films

The dynamics of changes in crack resistance as a result of accelerated aging processes modeling, as well as a diagram of changes in crack resistance depending on the radiation dose after aging are presented in Fig. 7. This technique has proved itself to be one of the most reliable methods for modeling natural aging processes as a result of long-term operation [41–43].

As can be seen from the data presented, the main changes in the crack resistance as a result of modeling aging processes for initial samples and irradiated with doses of

$10^{13}$–$10^{14}$ ion/cm$^2$ are associated with a decrease after 20–25 h of testing. Moreover, the maximum decrease in crack resistance is 25–45% of the initial values for these samples. In the case of samples irradiated with doses of $10^{15}$–$10^{16}$ ion/cm$^2$, this decrease does not exceed 5–10%, which indicates a good degree of resistance to long-term external influences.

Typical SEM images of the surface of thin films after aging tests are presented in Fig. 8. As can be seen from the data presented in the case of initial samples, the formation of branched microcracks and also strongly defective regions is observed on the surface of thin films after testing. The presence of such structural changes indicates the degradation
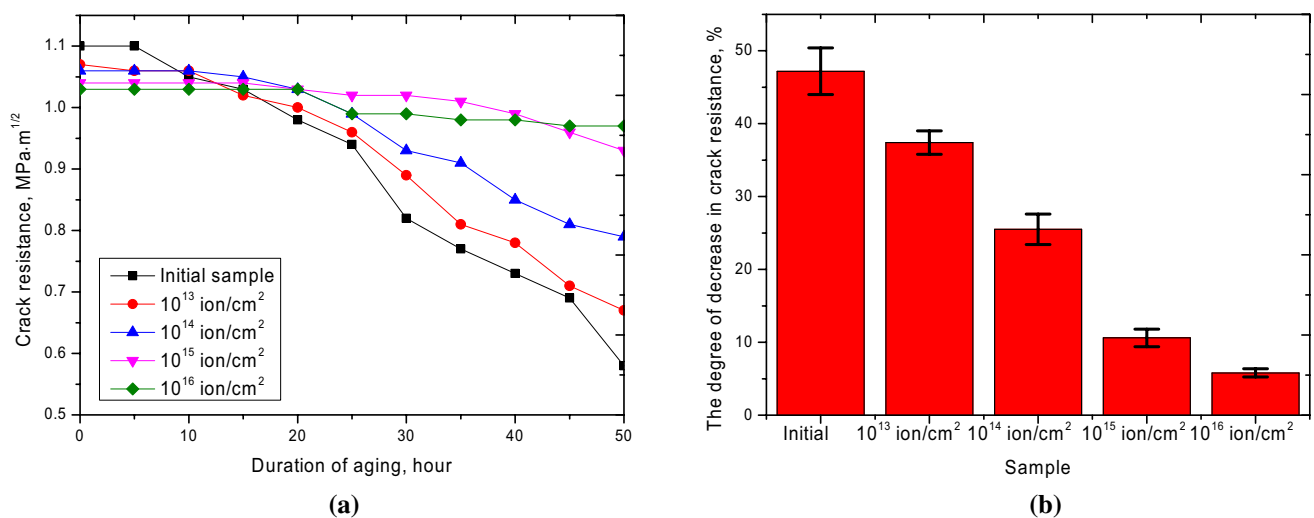


**(a)**



**(b)**

**Fig. 7** **a** Dynamics of changes in crack resistance as a result of modeling aging processes; **b** diagram of change in degree of crack resistance reduction

of thin films as a result of exposure to water vapor under pressure, simulating the aging effect. For irradiated samples, with an increase in the radiation dose, a decrease in the number of microcracks on the surface of the films is observed, and in the case of samples irradiated with $10^{15}$–$10^{16}$ ion/$cm^2$ microcracks are not observed. For samples irradiated with maximum doses, the main topographic changes in the surface are associated with an increase in surface roughness. Such behavior of changes in surface topography as a result of modeling the aging process indicates that, as a result of irradiation, a change in structural properties, in particular, an increase in the density of dislocations, leads not only to an increase in hardness, but also to an increase in crack resistance of thin films.

The results of a comparative analysis of the change in the band gap and the electrical conductivity of the films after modeling the aging effect are presented in Fig. 9.

As can be seen from the presented data, the greatest deterioration of both optical and conductive properties is observed for the samples in the initial state and irradiated with small doses of $10^{13}$–$10^{14}$ ion/$cm^2$, for which the greatest cracking of the surface layer in contact with water vapor was observed when modeling the aging effect. For samples irradiated with doses of $10^{15}$–$10^{16}$ ion/$cm^2$, the doping effect not only led to an increase in crack resistance, but also to a

decrease in the band gap and conductivity within the error, which indicates the high resistance of thin irradiated films to degradation and aging. The increase in aging resistance due to ionic modification is due to structural changes, as well as an increase in the density of dislocations in the surface layer and grain boundaries, as a result of crushing of crystallites and their reorientation. A change in the dislocation density leads to the formation of additional barriers that prevent the formation of microcracks in the structure as a result of external influences and further cracking of the surface layer. A similar behavior of increasing the resistance to external influences when thin films or multilayer coatings are present in the structure in the case of amorphous layers or a high dislocation density is shown in [49, 50].

## 4 Conclusion

In general, the results of the study show the promise of using ionizing radiation for the directed modification of structural, optical, mechanical properties, as well as increasing the resistance to external influences and the degradation of thin $TiO_2$ films. The dose dependences obtained for changing the properties of thin films will make it possible to use these data not only for a fundamental understanding of radiation
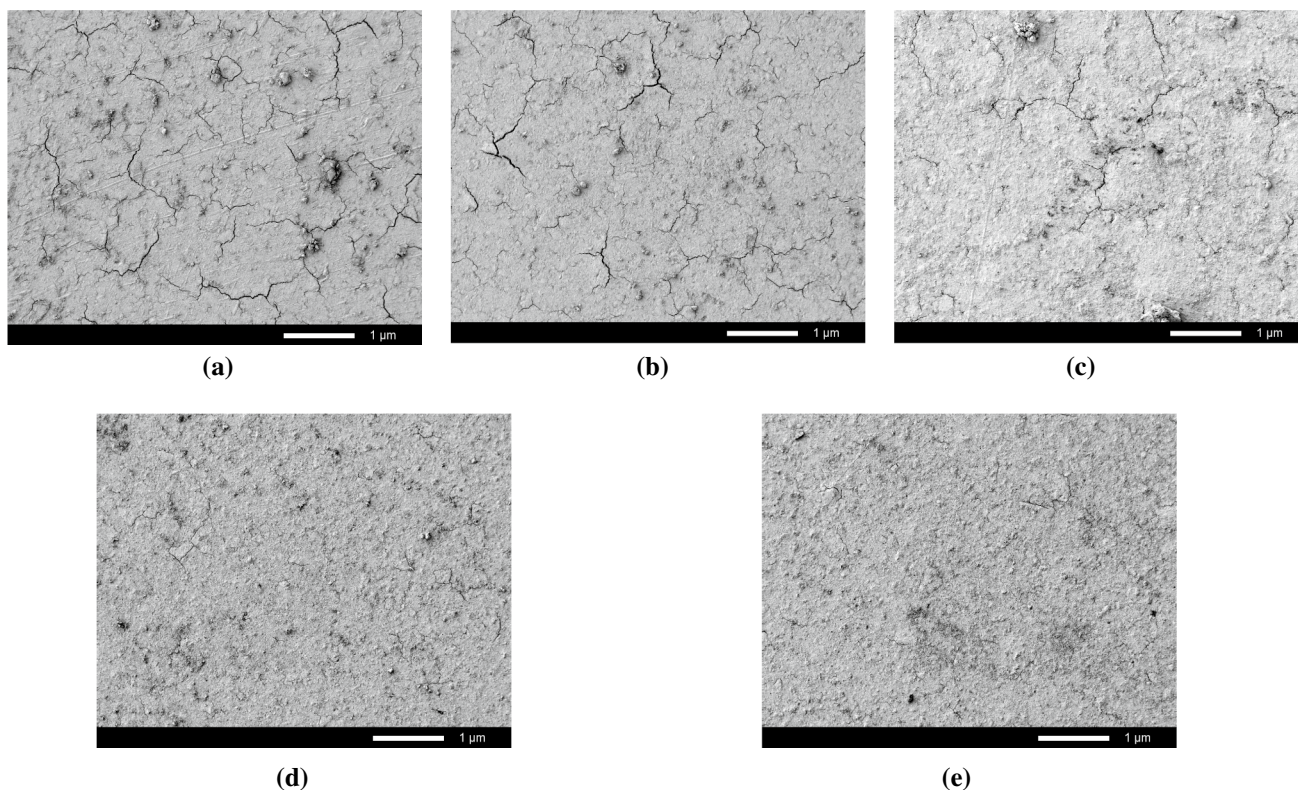


**Fig. 8** SEM images of the surface of thin films after modeling aging processes: **a** initial; **b** $10^{13}$ ion/$cm^2$; **c** $10^{14}$ ion/$cm^2$; **d** $10^{15}$ ion/$cm^2$; **e** $10^{16}$ ion/$cm^2$
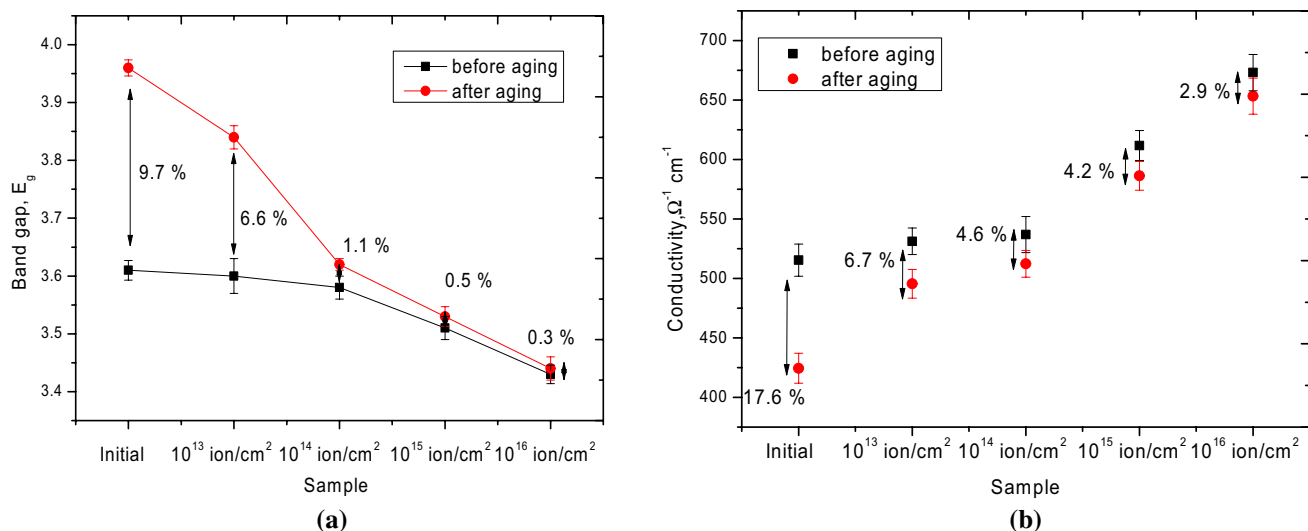
**Fig. 9** **a** Graph of comparison of variation of band gap width before and after aging of thin films; **b** Graph of comparison of variation of specific conductivity value before and after aging of thin films

hardening, but also for the application of low-energy ionizing radiation and the doping effect on an industrial scale. The established dependences of the change in optical properties, in particular, the band gap, of $TiO_2$ thin films can later be used to increase the efficiency of photocatalytic decomposition reactions, in which this value plays an important role. These changes in the mechanical and strength characteristics of thin films can be further used to model and calculate the operational characteristics of thin $TiO_2$ films as protective anticorrosion coatings.

## References

1. Kumar, V., et al. Study of humidity sensing properties and ion beam induced modifications in SnO2-TiO2 nanocomposite thin films. Surface Coatings Technol. (2020): 125768.

2. E.R. Shaaban et al., Dilute magnetic semiconductor of ZnCoSe thin films: structural, optical, and magnetic characteristics. J. Am. Ceram. Soc. **102**(7), 4067–4081 (2019)

3. C.-Y. Tsay et al., Microstructural and optical properties of Ga-doped ZnO semiconductor thin films prepared by sol–gel process. Thin Solid Films **519**(5), 1516–1520 (2010)

4. S.M. Rashwan, S.M. Abd El-Wahab, M.M. Mohamed, Electrodeposition and characterization of CdSe semiconductor thin films. J. Mater. Sci. **18**(6), 575–585 (2007)

5. K.K. Kadyrzhanov, K. Tinishbaeva, V.V. Uglov, Investigation of the effect of exposure to heavy Xe22+ ions on the mechanical properties of carbide ceramics. Eurasian Phys. Techn. J. **17**(33), 46–53 (2020)

6. Liu, Zhao, et al. "Strain engineering of oxide thin films for photocatalytic applications." *Nano Energy* (2020): 104732.

7. W. Zhang, D. Wang, W. Zheng, A semiconductor-electrochemistry model for design of high-rate Li ion battery. J. Energy Chem. **41**, 100–106 (2020)

8. A.A. Hssi et al., High-quality Cu 2 O thin films via electrochemical synthesis under a variable applied potential. J. Mater. Sci. **31**(5), 4237–4244 (2020)

9. J.-W. Choi et al., Tin oxysulfide composite thin films based on atomic layer deposition of tin sulfide and tin oxide using Sn (dmamp) 2 as Sn precursor. Ceram. Int. **46**(4), 5109–5118 (2020)

10. Makhlouf, Abdel Salam Hamdy, Adrian Perez, and Edgar Guerrero. Recent trends in smart polymeric coatings in biomedicine and drug delivery applications. In: Advances in smart coatings and thin films for future industrial and biomedical engineering applications. Elsevier, 2020. 359–381.

11. M.L. Coluccio et al., Emerging designs of electronic devices in biomedicine. Micromachines **11**(2), 123 (2020)

12. López-Suárez, A, et al. Optical, structural and electrical properties of ZnO thin films doped with Mn. J. Mater. Sci. (2020): 1–9.

13. N. Méndez-Lozano et al., Morphological study of $TiO_2$ thin films doped with cobalt by metal organic chemical vapor deposition. Res. Phys. **16**, 102891 (2020)

14. Gaukås, NH, et al. (2020) Ferroelectric and dielectric properties of Ca 2+-doped and Ca 2+–Ti 4+ co-doped K 0.5 Na 0.5 NbO 3 thin films. J Mater Chem C 8.15: 5102–5111.

15. Xiying Ma et al., Photoelectric characteristics of rare earth element Er doped molybdenum selenide thin films. J. Nanoelectron. Optoelectron. **15**(3), 384–388 (2020)

16. M. Pérez-González et al., Sol-gel synthesis of Ag-loaded TiO2-ZnO thin films with enhanced photocatalytic activity. J. Alloy. Compd. **779**, 908–917 (2019)

17. M.K. Tariq et al., Comparative study of Ag, Sn or Zn doped TiO2 thin films for photocatalytic degradation of methylene blue and methyl orange. Mater. Res. Exp. **6**(10), 106435 (2019)

18. M. Baradaran et al., The role of Al concentration on improving the photocatalytic performance of nanostructured ZnO/ZnO: Al/ZnO multilayer thin films. J. Alloy. Compd. **788**, 289–301 (2019)

19. A.M. Alotaibi et al., Enhanced photocatalytic and antibacterial ability of Cu-doped anatase TiO2 thin films: theory and experiment. ACS Appl. Mater. Interfaces **12**(13), 15348–15361 (2020)
20. S. Zhang et al., Excellent mechanical, tribological and anti-corrosive performance of novel Ti-DLC nanocomposite thin films prepared via magnetron sputtering method. Carbon **151**, 136–147 (2019)
21. V.I. Shymanski et al., Structure and phase composition of tungsten alloys modified by compression plasma flows and high-intense pulsed ion beam impacts. Appl. Surf. Sci. **491**, 43–52 (2019)
22. A.F. Zatsepin et al., Modification of MgAl 2 O 4 electron-optic properties by pulsed ion beam. Phys. At. Nucl. **82**(11), 1558–1564 (2019)
23. K. Mahmood et al., Surface, structural, electrical and mechanical modifications of pulsed laser deposited ZrN thin films by implantation of MeV carbon ions. Nuclear Instrum Methods Phys. Res. Sect. B **448**, 61–69 (2019)
24. A.I. Ryabchikov et al., Surface modification of Al by high-intensity low-energy Ti-ion implantation: microstructure, mechanical and tribological properties. Surface Coatings Technol. **372**, 1–8 (2019)
25. R. Wei, Low energy, high current density ion implantation of materials at elevated temperatures for tribological applications. Surface Coatings Technol. **83**(1–3), 218–227 (1996)
26. C. Bonafos et al., Manipulation of two-dimensional arrays of Si nanocrystals embedded in thin SiO 2 layers by low energy ion implantation. J. Appl. Phys. **95**(10), 5696–5702 (2004)
27. H. Shen et al., Visible-light photocatalysis of nitrogen-doped TiO2 nanoparticulate films prepared by low-energy ion implantation. Appl. Surface Sci. **253**(17), 7024–7028 (2007)
28. A.L. Stepanov, I.B. Khaibullin, Fabrication of metal nanoparticles in sapphire by low-energy ion implantation. Rev. Adv. Mater. Sci **9**(2), 109–129 (2005)
29. A. Hernández et al., Optical properties of porous GaAs formed by low energy ion implantation. Vacuum **171**, 108976 (2020)
30. X. Xiao, Yu. Long, Nano-indentation of ion-irradiated nuclear structural materials: a review. Nuclear Mater. Energy **22**, 100721 (2020)
31. C. Luo et al., Ionoluminescence and photoluminescence study of annealing and ion irradiation effects on zinc oxide. Nuclear Instrum. Methods Phys. Res. Sect. B **471**, 7–12 (2020)
32. N. Chuklina et al., Comparative quantum chemistry study of the F-center in lanthanum trifluoride. Nucl. Instrum. Methods Phys. Res., Sect. B **474**, 57–62 (2020)
33. L.N. Myasnikova et al., Computer simulations of the band structure and density of states of the linear chains of NaCl ions. Latvian J. Phys. Tech. Sci. **56**(4), 49–56 (2019)
34. K. Kimura, S. Sharma, A. Popov, Fast electron–hole plasma luminescence from track-cores in heavy-ion irradiated wide-band-gap crystals. Nucl. Instrum. Methods Phys. Res., Sect. B **191**(1–4), 48–53 (2002)
35. A. Lushchik et al., Influence of complex impurity centres on radiation damage in wide-gap metal oxides. Nucl. Instrum. Methods Phys. Res Sect. B **374**, 90–96 (2016)
36. A. Kozlovskiy et al., Structure and corrosion properties of thin TiO2 films obtained by magnetron sputtering. Vacuum **164**, 224–232 (2019)
37. A. Kozlovskiy et al., The study of the applicability of ionizing radiation to increase the photocatalytic activity of TiO2 thin films. J. Nanostruct. Chem. (2020). https://doi.org/10.1007/s40097-020-00353-x
38. A.J. Perry, H.K. Pulker, Hardness, adhesion and abrasion resistance of TiO2 films on glass. Thin Solid Films **124**(3–4), 323–333 (1985)
39. P.J. Martin et al., Deposition of TiN, TiC, and TiO2 films by filtered arc evaporation. Surf. Coat. Technol. **49**(1–3), 239–243 (1991)
40. M. Zheng et al., Preparation, structure and properties of TiO2–PVP hybrid films. Mater. Sci. Eng B **77**(1), 55–59 (2000)
41. A.O. Zhigachev et al., Low-temperature aging of baddeleyite-based Ca-TZP ceramics. J. Am. Ceram. Soc. **100**(7), 3283–3292 (2017)
42. G.K.R. Pereira et al., Low-temperature degradation of Y-TZP ceramics: a systematic review and meta-analysis. J. Mech. Behav. Biomed. Mater. **55**, 151–163 (2016)
43. G.K.R. Pereira et al., Mechanical behavior of a Y-TZP ceramic for monolithic restorations: effect of grinding and low-temperature aging. Mater. Sci. Eng. C **63**, 70–77 (2016)
44. V.D. Mote, Y. Purushotham, B.N. Dole, Williamson-Hall analysis in estimation of lattice strain in nanometer-sized ZnO particles. J. Theor. Appl. Phys. **6**(1), 6 (2012)
45. A.L. Kozlovskiy et al., Dynamics of radiation damage in AlN ceramics under high-dose irradiation, typical for the processes of swelling and hydrogenation. Crystals **10**(6), 546 (2020)
46. V. Kumar, R. Kumar, Low energy Kr5+ ion beam engineering in the optical, structural, surface morphological and electrical properties of RF sputtered TiO2 thin films. Opt. Mater. **91**, 455–469 (2019)
47. J.H. Evans, An interbubble fracture mechanism of blister formation on helium-irradiated metals. J. Nucl. Mater. **68**(2), 129–140 (1977)
48. F. Laatar et al., Effect of deposition temperature on the structural and optical properties of CdSe QDs thin films deposited by CBD method. Mater. Res. Bull. **78**, 83–95 (2016)
49. V.V. Uglov et al., Simulation of defect formation, amorphization and cluster formation processes in nc-TiN/a-Si3N4 nanocomposite under Xe irradiation. Comput. Mater. Sci. **143**, 143–156 (2018)
50. V.V. Uglov et al., Blister formation in ZrN/SiN multilayers after He irradiation. Surf. Coat. Technol. **344**, 170–176 (2018)